CrossMark

Strong absorption near exceptional points in plasmonic waveguide arrays

Shaolin Ke[1] · Jianxun Liu[2] · Qingjie Liu[2] · Dong Zhao[2,3] · Weiwei Liu[2]

Abstract

We investigate the exceptional points (EPs) in plasmonic waveguide arrays, including metallic waveguide arrays (MWAs) and graphene sheet arrays (GSAs). The EPs emerge at the boundary of strong and weak coupling ranges in both systems. The cross conversion of Bloch modes and variation of geometric phase can be observed by encircling an EP in the parametric space. We also show the Bloch modes exhibit strong absorption in the vicinity of EPs in GSAs, which originates from the enhanced longitude electric field along the propagation direction. The abnormal absorption and field enhancement also arise in ultrathin MWAs and disappear when the thickness of metal film increases. Our results may find applications in optical switches and sensors at the nanoscale.

Keywords Plasmonic waveguides · Exceptional points · Absorption · Field enhancement

1 Introduction

Surface plasmon polaritons (SPPs), supported at the interface of metal and dielectric, have attracted enormous interest on nanophotonics due to their subwavelength characteristic and extremely optical field confinement (Orlova et al. 2014; Sun et al. 2016; Wang et al. 2017a, 2018; Chen et al. 2018; Qin et al. 2016; Kou et al. 2013). Metallic waveguide arrays (MWAs) are extensively utilized to modulate the flow of SPPs due to their capability to engineer the dispersion relation (Orlova et al. 2014; Kou et al. 2013; Qin et al. 2018). With the emergence of new plasmonic materials, graphene has arisen as a promising candidate from terahertz to mid-infrared frequencies (Bao and Loh 2012; Wang et al. 2017b, c; Deng et al. 2015a, 2016; Zhao et al. 2017; Zhang et al. 2014). The SPPs in graphene manifest stronger field confinement when comparing with metals. The surface conductivity of graphene can be flexibly tuned via electrostatic and chemical doping (Bao and Loh 2012). The

✉ Weiwei Liu
lwhust@hust.edu.cn

1 Laboratory of Optical Information Technology, Wuhan Institute of Technology, Wuhan 430205, China

2 School of Physics, Huazhong University of Science and Technology, Wuhan 430074, China

3 School of Electronics Information and Engineering, Hubei University of Science and Technology, Xianning 437100, China

high carrier mobility in graphene makes it suitable for high speed light detection (Ni et al. 2016; He et al. 2018a, b; Li et al. 2018; Peng et al. 2017). Graphene sheets arrays (GSAs) are also proposed to manipulate the propagation of SPPs (Ge et al. 2015; Wang et al. 2017b).

One important issue to design plasmonic circuits is to carefully deal with optical loss, which may hamper the practical application. The optical gain by extra optical pumping or quantum dots are used to compensate or even reverse the propagation loss (De Leon and Berini 2010; Hong et al. 2018; Li et al. 2012; Hong et al. 2017; Xie et al. 2018; Lin et al. 2016). The system associated with gain or loss is non-Hermitian, which has been utilized to introduce novel functionalities to a variety of photonic devices (Lin et al. 2016; Ke et al. 2018). The gain and loss present in the system may greatly alter the optical response of systems, especially at the non-Hermitian singularities known as exceptional points (EPs) (Lee 2010; Ke et al. 2016). The eigenvalues and eigenstates of the system coalesce at EPs. In contrast, the degenerate points such as Dirac points (DPs) in Hermitian systems have same eigenvalues but different eigenstates (Deng et al. 2016b), (Ge et al. 2017). Many unusable phenomena are found associated with the EPs, such as loss induced transparency (Guo et al. 2009), unidirectional reflection (Feng et al. 2014; Huang et al. 2015), state exchange (Ke et al. 2016, 2017), and non-trivial geometric phase (Lee 2010). The EPs have been investigated in dielectric waveguides (Guo et al. 2009; Liu et al. 2016), multiple plasmonic waveguides (Alaeian and Dionne 2014), and ring resonators (Hodaei et al. 2017).

In this work, we investigate the EPs in MWAs and GSAs. The EPs appear at the boundary of strong and weak coupling ranges in both systems. The influence of loss on the SPP dispersion relations and Bloch modes is usually neglected as the imaginary part of the permittivity of metal is fairly small when compared to its real part. Here, we show the influences are prominent near the EPs. We compare the optical property of GSAs and MWAs and show that they are consistent with each other when the thickness of metal film is extremely small. The Bloch modes are of strong propagation loss near the EPs in GSAs or in ultrathin MWAs. The study may benefit to understanding the relation between MWAs and GSAs.

2 EPs in metallic waveguide array

We start to investigate the Bloch modes in MWAs. Figure 1a show the geometric diagram of MWAs. The metal films (Au) are spatially separated and embedded in the host dielectric medium with the relative permittivity denoted by ε_d. For simplicity, we consider the dielectric is air with $\varepsilon_d = 1$. The thickness of metal film and dielectric is represented as t_m and t_d, respectively. The period of array is $d = t_m + t_d$. The incident wavelength is fixed at $\lambda = 0.8$ μm. The relative permittivity of metal is figured out as $\varepsilon_m = -8.67 + 0.96i$ [CRC].

We investigate the transverse magnetic (TM) polarized collective SPP modes propagating along z direction, which are referred as Bloch modes in the periodic configuration. The dispersion relation of MWAs is given by (Kou et al. 2013)

$$\cos \varphi = \cos(k_1 t_d) \cos(k_2 t_m) - \frac{\varepsilon_m k_1^2 + \varepsilon_d k_2^2}{2\varepsilon_m \varepsilon_d k_1 k_2} \sin(k_1 t_d) \sin(k_2 t_m), \tag{1}$$

where φ is the Bloch momentum, $k_1 = (k_z^2 - \varepsilon_d k_0^2)^{1/2}$ and $k_2 = (k_z^2 - \varepsilon_m k_0^2)^{1/2}$ with k_z denoting the propagation constant of SPPs. Figure 1b shows k_z as a function of Bloch momentum and period. The loss of metal is neglected and thus the system is Hermitian.
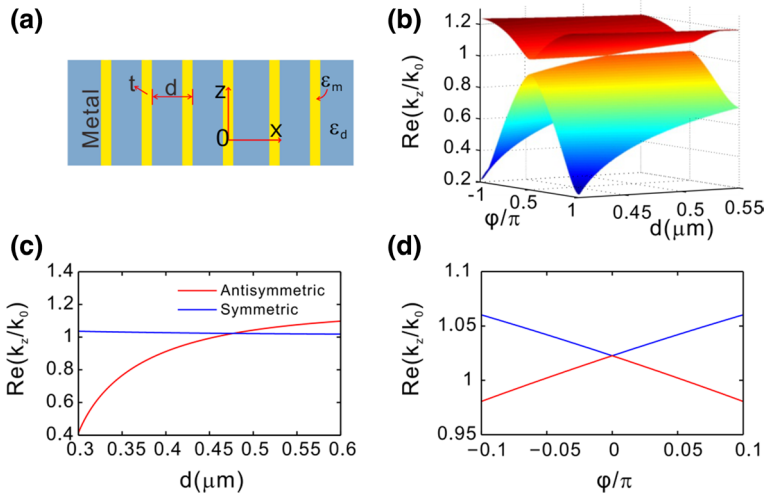
Fig. 1 Dirac point in MWAs without considering the loss. **a** Schematic of MWAs. **b** The dispersion relation $k_z(\varphi)$ as a function of period d. **c** The propagation contestants for varying d at $\varphi = \varphi_{DP}$. **d** The dispersion relation at $d = d_{DP}$

The thickness of metal is chosen as $t = 20$ nm. There are two bands supported in MWAs, which coalesce at the DP. The DP is a degenerate point as the mode profiles of Bloch modes are different. The DP locates at center of Brillouin zone when the averaged permittivity is vanished (Kou et al. 2013; Deng et al. 2015a, 2016a, b), that is,

$$\varepsilon_m t_m + \varepsilon_d t_d = 0 \tag{2}$$

The location of DP is denoted as (φ_{DP}, d_{DP}), which is (0, 477.4 nm) for the parameter we choose. To clearly see the DP, we plot the curves $k_z(d)$ at $\varphi = 0$ in Fig. 1c and $k_z(\varphi)$ at $d = 0$ in Fig. 1d. The magnetic fields of Bloch modes are symmetric or antisymmetric as $\varphi = 0$. The band gap closes at DP and opens for other parameters, indicating the band inversion and topological phase transition (Deng et al. 2016b; Wang et al. 2018). Moreover, one can find the dispersion relation is linear in the vicinity of DP, which can lead the diffraction-free and self-splitting beam propagation (Deng et al. 2015b). Previous studies have reported the existence of DPs in MWAs (Kou et al. 2013; Deng et al. 2016b). However, they neglect the influence of the loss of metal. Actually, a single DP will split into two EPs when the intrinsic loss of metal is taken into account. The dispersion relation would be greatly altered in this range as well.

Figure 2 shows the dispersion relation of MWAs at $d = d_{DP}$ as the loss of metal is considered. The dispersion relation is greatly changed when compared with Fig. 1d. The system now becomes non-Hermitian and the propagation constants are complex-valued. The real and imaginary part of propagation constants coalesce at the same time for $\varphi = \varphi_{EP} = \pm 0.02\pi$, which indicates the appearance of EPs. The EPs separate the dispersion relation into two regions: inside two EPs ($\varphi < |\varphi_{EP}|$), $\mathrm{Re}(k_z)$ are flat and degenerate. Outside two EPs ($\varphi > |\varphi_{EP}|$), $\mathrm{Im}(k_z)$ are flat and degenerate. The feature is familiar with the variation of a square root of multi-value function in complex analysis (Zhen et al. 2015).
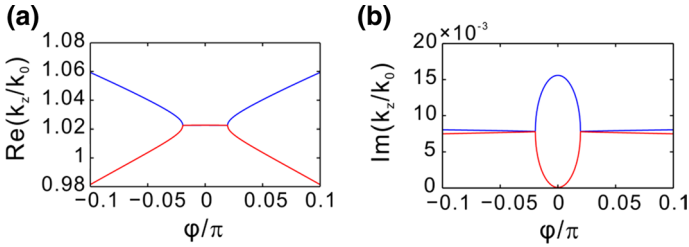
(a)

(b)

Fig. 2 Exceptional points in MWAS. **a** The real and **b** imaginary parts of propagation constants in the vicinity of Brillouin zone at $d = 477.4$ nm

3 General property of EPs

There are two sets of eigenfunctions in non-Herimitian systems, including the left $\langle \psi_n |$ and right $| \psi_n \rangle$ eigenfunctions. The two Bloch modes are no longer orthogonal in the non-Hermitian systems. Instead, they are biorthogonal in the sense of an unconjugated "inner product" between left and right eigenstates, $\langle \psi_m | \psi_n \rangle = \delta_{mn}$ where m and n represent mode number (Lee 2010). The biorthogonality holds generally, but breaks down at EPs. When the system operates away from EP, the inner product is zero for two different modes (m·n) and is unity for the same mode (m=n). When approaching EP, the relation $\langle \psi_m | \psi_n \rangle = \delta_{mn}$ does not hold. At the EPs, the two eigenstates coalesce and become self-orthogonal. As a result, the inner product is vanished. Such a property is usually qualified by the phase rigidity, which is defined based on inner product and given as $r_m = \langle \psi_m | \psi_m \rangle$ (Lee 2010; Ding et al. 2015). The absolute value of phase rigidity is unity when the system operates away from EPs and it is vanished when approaching EPs. In the calculation, the magnetic fields (H_y) serve as right eigenstates and the left eigenstates is defined as $\langle \psi | = H_y^*(\varepsilon^*)$. Then, the phase rigidity is $r = \int H_y^*(\varepsilon^*) H_y(\varepsilon) dx$, where the integration is limited in one period ($-d/2 < x < d/2$). Figure 3 shows the phase rigidity of two Bloch modes as a function of Bloch momentum at $d = d_{DP}$. The blue and red lines represent two different modes. The phase rigidity tends to be zero at EPs and unity when away from the EPs.

We further explore the topological nature of EPs, which can be studied by encircling the EP in the parameter space. Two parameters should be turned at the least. Here, the parameters are chosen as period d and Bloch momentum φ. A loop (A · B · C · D · A) is created in the parameter space as shown in Fig. 4a, which encloses an EP ($\varphi_{EP} = 0.02\pi, d_{EP} = 477.4$ nm). For each point along the loop, the waveguide arrays have certain period and Bloch momentum. Then, we can numerically calculate the two eigenvalues of Bloch modes according to Eq. (1). Figure 4b presents the evolution of eigenvalues along the loop. The blue and red dots denote the initial values of two eigenvalues at starting point A ($d = 490$ nm, $\varphi = 0$). Following the

Fig. 3 Phase rigidity in the vicinity of EPs. The period of MWAs is $d = d_{DP}$
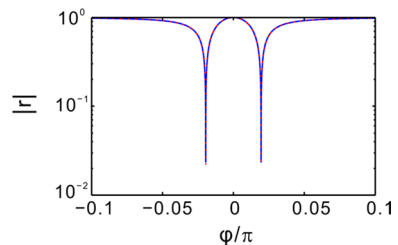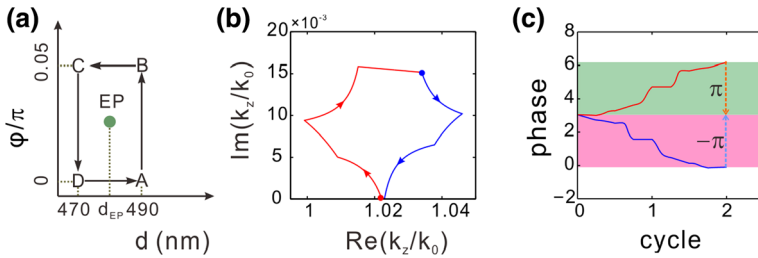
Fig. 4 Topological property of EPs. **a** The parametric loop that encloses an EP. **b** The evolution of eigenvalues along the loop. The different colors represent different modes. **c** Phase evolution of eigenmodes (H_y) at $x=0$. The blue line is for the parameters changing along clockwise loop, while the red one for anticlockwise loop. (Color figure online)

loop, the two complex eigenvalues switch their positions when the system returns to its initial parameters. In contrast, two eigenvalues come back to themselves at the end of the loop if the EP is not enclosed in the loop. The mode exchange is caused by the topological structure of complex eigenvalues near the EP as it exhibits the same geometric property as that of branch point of complex multi-value function. Furthermore, such unique property can be used for mode switching (Lee 2010; Ke et al. 2016).

During the encircling progress, the corresponding eigenmodes should also exchange their identity. After two cycle loops encircling an EP with same orientation, both modes return to themselves. Moreover, each mode picks up a phase change, which is referred as geometric phase (Lee 2010; Ke et al. 2016). Usually, one can't directly extract geometric phase from the eigenmodes as they possess arbitrary phase obtained from Maxwell equations. The arbitrary phase is dismissed by a continuous phase-plot of eigenstates (Lee 2010), which requires the inner product $\mathrm{Im}(\langle \psi^* n|\psi_n\rangle)=0$. Then, the geometric phase can be extracted from phase difference between the initial $|\psi_n\rangle_I$ and final states $|\psi_n\rangle_F$ at start and end of the loop. The geometric phase is an integer multiple of π, which is independent of position. We trace the phase of magnetic field (H_y) of one Bloch mode at position $x=0$. The result is illustrated in Fig. 4c. The non-trivial geometric phase can be observed by encircling an EP twice, which is $-\pi$ for clockwise loops and π for anticlockwise loops.

4 EPs in graphene waveguide arrays

We now consider the EPs in GSAs. A diagram of GSAs is displayed in Fig. 5a. The monolayer graphene sheets are spatially separated with period d and embedded in the host dielectric medium with the relative permittivity denoted by ε_d. Here we consider the dielectric is air with $\varepsilon_d=1$ for simplicity. The surface conductivity of graphene σ_g can be modeled using Kubo formula (Huang et al. 2017; Wang et al. 2012), which relates to the frequency ω, chemical potential μ_c, momentum relaxation time τ and temperature T. In this work, the chemical potential is fixed at $\mu_c=0.15$ eV and the momentum relaxation time is chosen as $\tau=0.5$ ps at room temperature ($T=300$ K). The incident wavelength is assumed to be $\lambda=10$ μm. The dispersion relation of SPPs under TM polarization is given by (Wang et al. 2012)

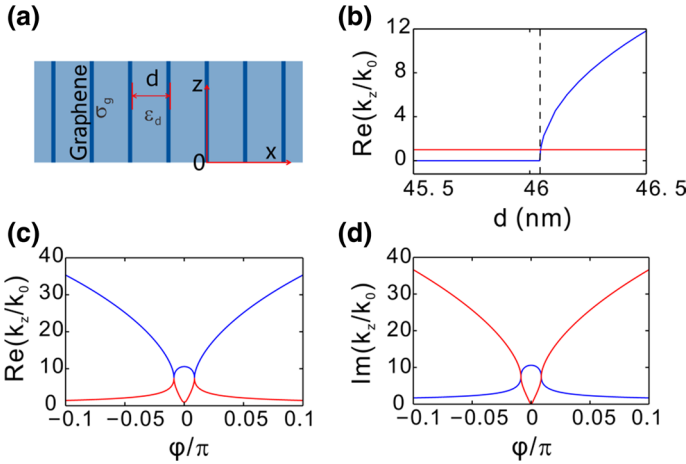$$\cos(\varphi) = \cosh(\kappa d) - \frac{\kappa \xi}{2}\sinh(\kappa d), \tag{3}$$

Fig. 5 The EPs in GSAs. **a** The schematic of GSAs. **b** The propagation constants as a function of period d at $\varphi = 0$ without considering the graphene loss. **c, d** The real and imaginary part of dispersion relation at $d = 46$ nm when the loss of graphene is taken into account

where φ represents the Bloch momentum, $\xi = \eta_0 \sigma_g / (i \varepsilon_d k_0)$ characterizes the effective mode width of SPPs in a single-layer graphene sheet with η_0 denoting the impedance and k_0 the wave vector of air, and $\kappa = (k_z^2 - \varepsilon_d k_0^2)^{1/2}$ with k_z being the propagating constant of Bloch mode.

Figure 5b illustrates the propagation constants for varying the array period at the center of Brillouin zone ($\varphi = 0$). The loss is not considered in the calculation. There are two modes supported in the system. However, the symmetric mode that supported in MWAs now becomes a trivial one with the propagation constants being $k_z = k_0$. This is due to the two-dimensional property of graphene. The result is similar to the case of MWAs. A DP arises at $d_{DP} = \xi$ as the two modes possess the same propagation constant. The location of DP is exactly at the position when the period is equal to plasmonic mode width (Wang et al. 2012). In general, the strong and weak couplings are distinguished according the mode width. Here, the location of DP exactly locates at the boundary of two regions. The same phenomenon also appears in MWAs if the thickness of metal films approaches to zero. To understand the distinction of strong and weak coupling is important in design of plasmonic waveguides. The coupled mode theory can be used in weak coupling region (Ke et al. 2018), while the effective index theory is introduced in the strong coupling one (Zhang et al. 2014). The location of DP in GSAs is accommodated with Eq. 2 when treating graphene as ultrathin metal films. The thickness of graphene is denoted as Δ and a relative equivalent permittivity of graphene is given by $\varepsilon_g = 1 + i \sigma_g \eta_0 / (k_0 \Delta)$ (Wang et al. 2012). Then, the critical condition for the emergence of DP is derived as

$$(d_{DP} - \Delta)\varepsilon_d + \Delta \varepsilon_g = 0. \tag{4}$$

Figures 5c, d plot the real and imaginary parts of dispersion relation at $d = d_{DP}$. The loss of graphene now is taken into account. Since the complex band structures of the system possess mirror symmetry, the EPs always appear in pairs. The two modes coalesce at $\varphi = \varphi_{EP} = \pm 0.0086\pi$. The shape of curve $k_z(\varphi)$ is different from that in Fig. 2. The real and imaginary parts of propagation constants are not degenerate at both inside

and outside the EPs. The similar phenomenon appears in MWAs with ultrathin thickness, indicating that the influence of loss becomes more significant.

We now try to figure out the location of EPs (d_{EP}, φ_{EP}) in GSAs. The value of period is approximately as $d_{EP} = \mathrm{Re}(\xi)$ as EP originates from DP with account of the loss. We further use perturbation method to solve Eq. (3) and find out the Bloch momentum φ_{EP}. At the center of Brillouin zone ($\varphi = 0$), the dispersion relation is simplified to

$$e^{-\kappa d} = (2 - \kappa\xi)/(2 + \kappa\xi). \tag{5}$$

Equation (5) have two solutions, the first one is trivial solution $\kappa_{10} = 0$. The second solution is figured out by using Padé approximation, which is

$$e^{-\kappa d} \approx \left(1 - \frac{d\kappa}{2} + \frac{d^2\kappa^2}{12}\right) \Big/ \left(1 + \frac{d\kappa}{2} + \frac{d^2\kappa^2}{12}\right). \tag{6}$$

Then, the second solution reads as $\kappa_{20} \approx \sqrt{12(d - \xi)/(d^2\xi)}$. In the vicinity of Brillouin center $\varphi = \Delta\varphi \ll 1$, the solution of Eq. (3) can be calculated by using perturbation method, which are

$$\kappa_1^2 \approx \frac{i\Delta\varphi^2}{-\mathrm{Re}(\xi)\mathrm{Im}(\xi)}, \kappa_2 \approx \kappa_{20} + \frac{\Delta\varphi^2}{(\xi - 2d)\sinh(\kappa_{20}d) + \kappa_{20}d\xi\cosh(\kappa_{20}d)} \tag{7}$$

Now, we try to figure out the location of exceptional point (d_{EP}, φ_{EP}). The period should be $d_{EP} = \mathrm{Re}(\xi)$ as EPs appear in the vicinity of DPs. When $d = d_{EP}$, we have $\sinh(\kappa_{20}d_{EP})$ $\approx \kappa_{20}d_{EP} + (\kappa_{20}d_{EP})^3/6$ and $\cosh(\kappa_{20}d_{EP}) \approx 1 + (\kappa_{20}d_{EP})^2/2$ as the term $\kappa_{20}d_{EP} \ll 1$. Then, the second equation of Eq. (7) becomes

$$\kappa_2 = a(1 + i) + \Delta\varphi^2\left\{1i \cdot \left[\frac{2}{3}\mathrm{Re}(\xi)a^3d_{EP}^3 + \mathrm{Im}(\xi)\left(2ad_{EP} - \frac{4}{3}a^3d_{EP}^3\right)\right]\right.$$
$$\left. - \left[\frac{2}{3}\mathrm{Re}(\xi)a^3d_{EP}^3 + \mathrm{Im}(\xi)\left(2ad_{EP} + \frac{4}{3}a^3d_{EP}^3\right)\right]^{-1}\right\}, \tag{8}$$

where $a = \sqrt{-6\mathrm{Im}(\xi)\mathrm{Re}(\xi)}/\mathrm{Re}(\xi)^2$. For the parameter we choose, one can find $\mathrm{Im}(\xi) \ll \mathrm{Re}(\xi)$. Therefore, the term $ad_{EP} = \sqrt{-6\mathrm{Im}(\xi)/\mathrm{Re}(\xi)} \ll 1$ and the high order term can be ignored as $a^3d_{EP}^3 \ll ad_{EP}$. Then, Eq. (8) is simplified to

$$\kappa_2 = a(1 + i) - \frac{3\Delta\varphi^2}{4a^3\mathrm{Re}(\xi)^4 + 12a\mathrm{Im}(\xi)\mathrm{Re}(\xi)}(1 + i), \tag{9}$$

At EP, two eigenvalues should be of equal values, that is, $\kappa_1^2 = \kappa_2^2$, which leads to $\Delta\varphi = \pm b\mathrm{Im}(\xi)/\mathrm{Re}(\xi)$ and $b = \sqrt[4]{288}$. Recalling the relation $\xi = -i\eta_0\sigma_g/(\varepsilon_d k_0)$, we arrive at

$$\varphi_{EP} = b\frac{\mathrm{Re}(\sigma_g)}{\mathrm{Im}(\sigma_g)}, \tag{10}$$

Equation (10) states that φ_{EP} only relates to the property of graphene, which is proportional to the ratio of real part and imaginary part of surface conductivity. The constant before Eq. (10) does not coincide well with the numerical results calculated by Eq. (1). We redefine the constant b by the data fitting, which is determined as $b = 5.44$. Then, the results indicated by Eq. (10) agree well with the numerical results as shown in Fig. 6. Therefore, the location of EPs can be flexibly tuned.
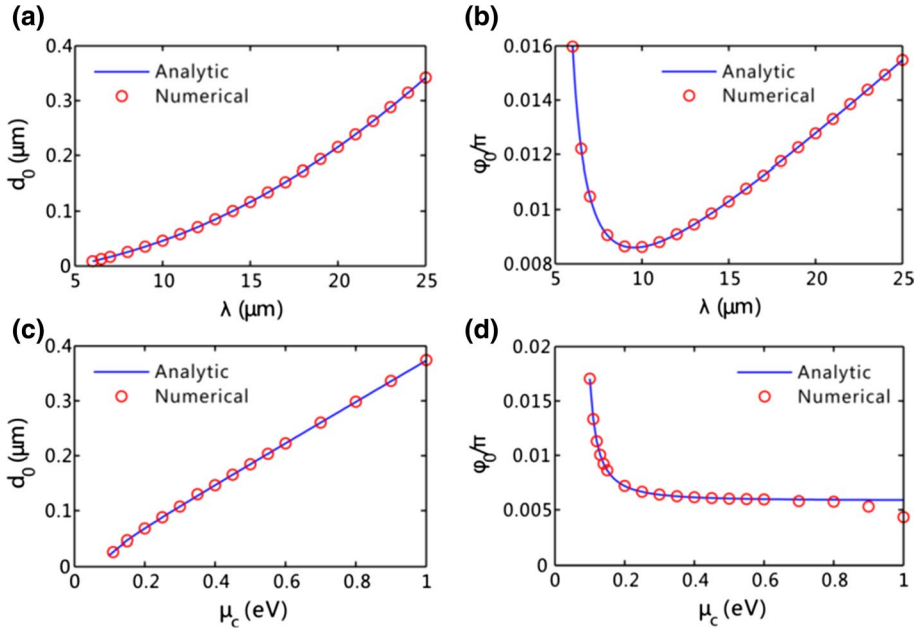
(a)

(b)

(c)

(d)

Fig. 6 The location of EPs for different parameters. **a**, **b** The position of EPs for varying incident wavelength. **c**, **d** The position of EPs for various chemical potential

Figures 6a, b show the location of EP as the incident wavelength is varied. The line represents the results directly calculated by the dispersion relation and the dots are the analytical results. One can see d_{EP} monotonically increase with the increase of incident wavelength. At the same time, φ_{EP} firstly decreases and then increases as the incident wavelength increases. Figures 6c, d illustrate the location of EP as the chemical potential is varied. One can see d_{EP} increases and φ_{EP} drops with the increase of chemical potential. The numerical results coincide fairly well with the theoretical indications.

5 Strong absorption in the vicinity of EPs

The propagating modes in GSAs possess large imaginary part in the vicinity of EPs as they are strongly mixed with the radiation ones. The real part of propagation constants k_z relates to effective index of SPP mode as $n_{eff} = real(k_z)/k_0$ and the imaginary part represents the propagation loss with absorption coefficient given by $\alpha = 2Im(k_z)$. To clearly see the absorption of propagating SPP mode in GSAs, we plot the curves $\alpha(d)$ for various Bloch momentums in Fig. 7a. When Bloch momentum equals to 0.01π, the absorption manifests a pronounced peak at $d = 46.26$ nm. As φ increases, the peak dramatically decreases and the position of peak shifts to larger period. Figure 7b presents the absorption coefficient as a funtion of Bloch momentum with $d = 30$ nm, 47 nm, and 60 nm. As $d = 47$ nm, $\alpha(\varphi)$ exhibits a distinct peak at Brillouin zone center and the maximum of absorption coefficient is 7.76 μm^{-1}. As d increases, the peak significantly decreases. On the other hand, GSAs locates at strong coupling region with smaller period ($d = 30$ nm). The Bloch modes
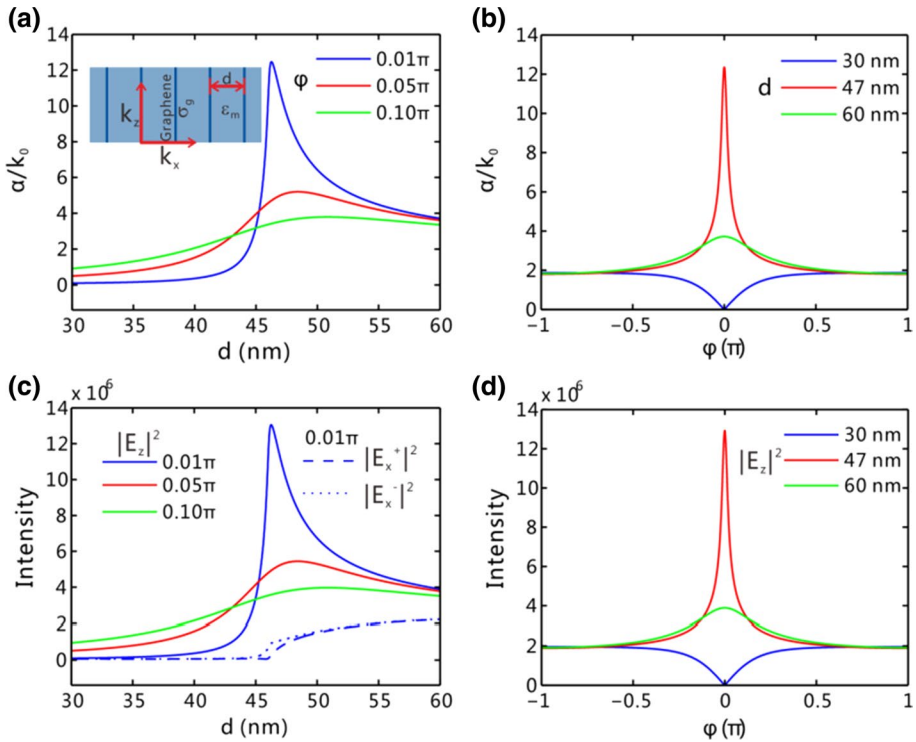
Fig. 7 The absorption coefficient α and the field intensity of Bloch modes in GSAs. **a** $\alpha(d)$ curves for different Bloch momentums, **b** $\alpha(\varphi)$ curves for different periods, **c, d** the field intensity at the graphene corresponding to **a** and **b**, respectively

is of slight propagation loss in entire Brillouin zone and the absorption coefficient displays a minimum at Brillouin center. Therefore, the maximum absorption of propagating mode will be limited to the value at $d = \xi$ and $\varphi = 0$.

To explain such a strong absorption, we investigate the electric field distributions in the GSAs. The magnitude field between graphene sheets $(-d < x < 0)$ is given by

$$H_y = A^+\exp[-\kappa(x+d)] + A^-\exp(\kappa x), \quad -d < x < 0 \tag{11}$$

The relation between amplitude A^+ and A^- can be determined by boundary condition and Bloch theorem (Wang et al. 2012), which is given by $A^+ = \frac{\exp(-\kappa d)\exp(ik_x d)-1}{\exp(ik_x d)-\exp(-\kappa d)}A^-$. Accordingly, the electric fields can be acquired as $E_x = -i\eta_0/(\varepsilon_d k_0)\cdot H_y/\cdot z$ and $E_z = i\eta_0/(\varepsilon_d k_0)\cdot H_y/\cdot x$.

The longitude component of electric field $|E_z|^2$ is continuous across graphene, while the transverse one $|E_x|^2$ undergoes a sudden change at the interface of graphene and dielectric. Therefore, as illustrated in Fig. 7c, we plot $|E_z|^2$ as a function period at the position of graphene and $|E_x|^2$ at the two interfaces of graphene. The dependence of longitude electric field on period d is accordant with that of absorption coefficient shown in Fig. 7a, while the transverse one shows no relevance. So we conclude that propagation loss of Bloch mode is the result of enhanced longitude field E_z, and the propagation loss is almost proportional to $|E_z|^2$. The longitude fields as a function of Bloch momentum also agree well with the proportional

relation to absorption coefficient as shown in Fig. 7d. The maximum value of electric field of propagating mode will be limited to the value at $E_z(\varphi=0, d=\xi)$ as well.

When the Bloch wavevector is $k_x=0$, the amplitude satisfy $A^-=-A^+$. By setting $A^-=1$, the field in GSAs is given by

$$H_y = -\exp[-\kappa(x+d)] + \exp(\kappa x), \quad -d < x < 0$$
$$E_z = \frac{i\eta_0\kappa}{k_0\varepsilon_d}\exp[-\kappa(x+d)] + \frac{i\eta_0\kappa}{k_0\varepsilon_d}\exp(\kappa x), \quad -d < x < 0 \tag{12}$$
$$E_x = -\frac{\eta_0 k_z}{\varepsilon_d k_0}\exp[-\kappa(x+d)] + \frac{\eta_0 k_z}{\varepsilon_d k_0}\exp(\kappa x), \quad -d < x < 0$$

The field should be normalized by the power, which is defined by $P=1/2\int_{-d}^{0}\mathrm{Re}\left(E_x H_y^*\right)\mathrm{d}x$.

Now we try to figure out the maximum electric field of propagating mode. We first consider the case without considering the intrinsic loss of graphene. The power is calculated by

$$P = \frac{\eta_0 k_z}{2\varepsilon_d k_0}\left[\frac{1-\exp(-2\kappa d)}{\kappa} - 2d\exp(-\kappa d)\right] \tag{13}$$

On the other hand, the longitude electric field at graphene ($x=0$) should be

$$E_z(x \to 0^-) = \frac{i\eta_0\kappa}{k_0\varepsilon_d}[\exp(-\kappa d)+1] \tag{14}$$

When the fields are normalized by setting $P=1$ W/m, the longitude electric field should be

$$\tilde{E}_z(x \to 0^-) = \frac{i\eta_0\kappa[\exp(-\kappa d)+1]}{\sqrt{\frac{\eta_0 k_0 k_z \varepsilon_d}{2}\left[\frac{1-\exp(-2\kappa d)}{\kappa} - 2d\exp(-\kappa d)\right]}} \tag{15}$$

The absolute value of square of longitude electric field is given by

$$|\tilde{E}_z|^2 = \frac{2\eta_0}{k_0\varepsilon_d}\frac{\kappa^3(\exp(-\kappa d) + 1)^2}{k_z\left[1 - \exp(-2\kappa d) - 2\kappa d\exp(-\kappa d)\right]} \tag{16}$$

In the vicinity of Dirac point ($\varphi=0$, $d \cdot \xi$), the wavevector should be $\kappa \cdot 0$ and $k_z = \sqrt{\varepsilon_d k_0^2 + \kappa^2} \to \varepsilon_d^{1/2}k_0$. One can find the limitation

$$\lim_{\kappa\to 0, d\to\xi}\frac{1 - \mathrm{e}^{-2d\kappa} - 2d\mathrm{e}^{-d\kappa}\kappa}{\kappa^3} = \frac{\xi^3}{3} \tag{17}$$

Applying Eq. (17) into Eq. (16), we arrive at

$$|\tilde{E}_z|^2 = \frac{24\eta_0}{\varepsilon_d^{3/2}k_0^2\xi^3}, \tag{18}$$

which indicates the longitude electric field at DPs. The lossless case is the ultimate limitation of E_z when the loss of graphene is reduced for larger relaxation time τ.

For lossy case, the express of power and the value of wavevector are different. The power is given by

$$P = \frac{\eta_0}{2\varepsilon_d k_0} \mathrm{Re}(k_z) \left(\frac{1}{\mathrm{Re}(\kappa)} - \frac{\exp(-2\mathrm{Re}(\kappa)d)}{\mathrm{Re}(\kappa)} - 2\exp(-\mathrm{Re}(\kappa)d)\frac{\sin(\mathrm{Im}(\kappa)d)}{\mathrm{Im}(\kappa)} \right) \quad (19)$$

which is accommodate with Eq. (13) as $\mathrm{Im}(\kappa)=0$. Because of the strong confinement of SPP in graphene, the wavevector of lossy case fulfill $\kappa \gg k_0$ and we have $k_z \cdot \kappa$. Moreover, the wavevector is approximated to be $\kappa \cdot [-6\mathrm{Im}(\xi)\mathrm{Re}(\xi)]^{1/2}/[\mathrm{Re}(\xi)]^2(1+i) = a(1+i)$ at $\varphi=0$ and $d=\mathrm{Re}(\xi)$. At this point, the square of normalized longitude electric field at graphene reads as

$$\left| \tilde{E}_z \right|^2 = \frac{24\eta_0}{\varepsilon_d k_0 \mathrm{Re}(\xi)\sqrt{-6\mathrm{Im}(\xi)\mathrm{Re}(\xi)}}. \quad (20)$$

It is found that $|E_z|^2$ indicated by Eq. (20) is 2.23×10^7 V^2/m^2, accommodating with the numerical value 2.21×10^7 V^2/m^2.

We now study absorption and field enhancement in the MWAs and focus at the influence of metal thickness t_m. Figure 8a shows the absorption coefficient as a function of period for different thickness of metal films. The Bloch momentum is fixed at $\varphi=0.02\pi$. As $t_m=2$ nm, the absorption shows a pronounced peak at $d=48.3$ nm. As the thickness
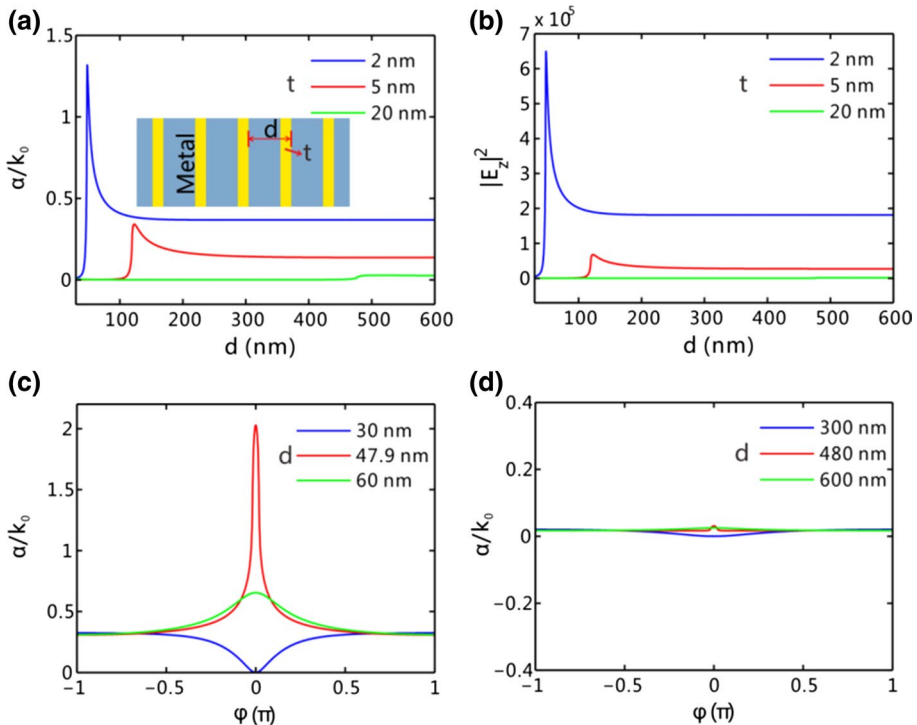

Fig. 8 The absorption coefficient and b the field intensity ($|E_z|^2$) of Bloch modes in MWAsy as a function of period for different thickness t. c, d are the $\alpha(\varphi)$ curves for $t=2$ nm and 20 nm, respectively

of metal film increases, the maximum of absorption coefficient decreases and the position of the maximum shifts to larger period d. The peak almost disappears as $t_m = 20$ nm. The transverse electric field intensity ($|E_z|^2$) at the interface of metal and dielectric is shown in Fig. 8b. The dependence of $|E_z|^2$ on period d is consistent with that of α. Therefore, the strong absorption and field enhancement only arise in thin metal. To further confirm the conclusion, Fig. 8c, d present $\alpha(\varphi)$ curves with respect to different periods at $t = 2$ nm and $t = 20$ nm, respectively. As $t = 2$ nm, the maximum absorption emerges at $d = 47.9$ nm in the Brillouin zone center. The maximum absorption will significantly decrease as period deviates from the critical value. On the other hand, at $t = 20$ nm, the loss of Bloch mode is relatively small in the whole Brillouin zone. The theory we develop for graphene can be utilized in MWAs when the metal films is thin enough. We adopt $\sigma_m = (\varepsilon_m - \varepsilon_d)k_0 t/(i\eta_0)$ to indicate the equivalent surface conductivity of thin metal. At this configuration, the maximum of longitude field indicated by Eq. (20) is $|E_z|^2 = 1.15 \times 10^6$ V^2/m^2 at $d = 47.7$ nm, which agrees well with the rigorous value 1.05×10^6 V^2/m^2. As the thickness of metal increases, the absorption is quite small as shown in Fig. 8d. Therefore, the strong absorption and field enhancement only emerge in GSAs or in MWAs with thin thickness. The study also provides useful information to deal with the propagation loss of SPPs in waveguide arrays. To avoid the strong loss of SPPs, one should choose thick metal films and other parameters such that the system performs away from EPs.

6 Conclusion

In conclusion, we have investigated the EPs in MWAs GSAs. The EPs emerges at the boundary of strong coupling and week coupling ranges, which can greatly alter the dispersion relation. The topological property of EPs, including the cross conversion of Bloch modes and variation of geometric phase, are studied by encircling an EP in the parametric space formed by Bloch momentum and period of structure. We show the Bloch modes exhibit strong propagation loss in the vicinity of EPs in GSAs or in MWAs with ultrathin metal films. The abnormal absorption can be explained by the enhanced longitude electric field along the propagation direction and we analytically calculated the limitation of maximum of enhanced field. The loss and field enhancement drop when the thickness of metal films increases. Our results may benefit to the design of plasmonic waveguides and find applications in optical switches and sensors at the nanoscale.

References

Alaeian, H., Dionne, J.A.: Non-Hermitian nanophotonic and plasmonic waveguides. Phys. Rev. B (2014). https://doi.org/10.1103/PhysRevB.89.075136

Bao, Q., Loh, K.P.: Graphene photonics, plasmonics, and broadband optoelectronic devices. ACS Nano **6**(5), 3677–3694 (2012)

Chen, J., Gan, F., Wang, Y., Li, G.: Plasmonic sensing and modulation based on Fano resonances. Adv. Opt. Mater. (2018). https://doi.org/10.1002/adom.201701152

De Leon, I., Berini, P.: Amplification of long-range surface plasmons by a dipolar gain medium. Nat. Photonics **4**(6), 382–387 (2010)

Deng, H., Ye, F., Malomed, B.A., Chen, X., Panoiu, N.C.: Optically and electrically tunable Dirac points and Zitterbewegung in graphene-based photonic superlattices. Phys. Rev. B (2015a). https://doi.org/10.1103/PhysRevB.91.201402

Deng, H., Chen, X., Malomed, B.A., Panoiu, N.C., Ye, F.: Transverse Anderson localization of light near Dirac points of photonic nanostructures. Sci. Rep. (2015b). https://doi.org/10.1038/srep15585

Deng, H., Chen, X., Malomed, B.A., Panoiu, N.C., Ye, F.: Tunability and robustness of Dirac points of photonic nanostructures. IEEE J. Sel. Top. Quantum Electr. (2016a). https://doi.org/10.1109/JSTQE.2016.2521711

Deng, H., Chen, X., Panoiu, N.C., Ye, F.: Topological surface plasmons in superlattices with changing sign of the average permittivity. Opt. Lett. **41**(18), 4281–4284 (2016b)

Ding, K., Zhang, Z.Q., Chan, C.T.: Coalescence of exceptional points and phase diagrams for one-dimensional PT-symmetric photonic crystals. Phys. Rev. B (2015). https://doi.org/10.1103/PhysRevB.92.235310

Feng, L., et al.: Demonstration of a large-scale optical exceptional point structure. Opt. Express **22**(2), 1760–1767 (2014)

Ge, L., Wang, L., Xiao, M., Wen, W., Chan, C.T., Han, D.: Topological edge modes in multilayer graphene systems. Opt. Express **23**(17), 21585–21595 (2015)

Ge, L., Liu, L., Xiao, M., Du, G., Shi, L., Han, D., Chan, C.T., Zi, J.: Topological phase transition and interface states in hybrid plasmonic–photonic systems. J. Opt. **19**(6), 1–5 (2017)

Guo, A., Salamo, G.J., Duchesne, D., Morandotti, R., Volatier-Ravat, M., Aimez, V.: Observation of PT-symmetry breaking in complex optical potentials. Phys. Rev. Lett. (2009). https://doi.org/10.1103/PhysRevLett.103.093902

He, L., Zhang, Q., Lan, P., Cao, W., Zhu, X., Zhai, C., Wang, F., Shi, W., Li, M., Bian, X., Lu, P., Bandrauk, A.: Monitoring ultrafast vibrational dynamics of isotopic molecules with frequency modulation of high-order harmonics. Nat. Commun. (2018a). https://doi.org/10.1038/s41467-018-03568-3

He, M., Li, Y., Zhou, Y., Li, M., Cao, Y., Lu, P.: Direct visualization of valence electron motion using strong-field photoelectron holography. Phys. Rev. Lett. (2018b). https://doi.org/10.1103/PhysRevLett.120.133204

Hodaei, H., Hassan, A.U., Wittek, S., Garcia-Gracia, H., El-Ganainy, R., Christodoulides, D.N., Khajavikhan, M.: Enhanced sensitivity at higher-order exceptional points. Nature **548**, 187–191 (2017)

Hong, Z., Rezvani, S., Zhang, Q., Lu, P.: Octave-spanning energy-scalable CEP-stabilized pulses from a dual-chirped noncollinear optical parametric amplifier. Opt. Quantum Electron. (2017). https://doi.org/10.1007/s11082-017-1209-y

Hong, Z., Zhang, Q., Rezvani, S.: Tunable few-cycle pulses from a dual-chirped optical parametric amplifier pumped by broadband laser. Opt. Laser Technol. **98**, 169–177 (2018)

Huang, Y., Veronis, G., Min, C.: Unidirectional reflectionless propagation in plasmonic waveguide-cavity systems at exceptional points. Opt. Express **23**(23), 29882–29895 (2015)

Huang, H., Ke, S., Wang, B., Long, H., Wang, K., Lu, P.: Numerical study on plasmonic absorption enhancement by a rippled graphene sheet. J. Lightwave Technol. **35**(2), 320–324 (2017)

Ke, S., Wang, B., Qin, C., Long, H., Wang, K., Lu, P.: Exceptional points and asymmetric mode switching in plasmonic waveguides. J. Lightwave Technol. **34**(22), 5258–5262 (2016)

Ke, S., Wang, B., Long, H., Wang, K., Lu, P.: Topological mode switching in a graphene doublet with exceptional points. Opt. Quantum Electron. **49**(224), 1–12 (2017)

Ke, S., Zhao, D., Liu, Q., Wu, S., Wang, B., Lu, P.: Optical imaginary directional couplers. J. Lightwave Technol. **36**(12), 2510–2516 (2018)

Kou, Y., Ye, F., Chen, X.: Multiband vector plasmonic lattice solitons. Opt. Lett. **38**(8), 1271–1273 (2013)

Lee, S.-Y.: Geometrical phase imprinted on eigenfunctions near an exceptional point. Phys. Rev. A (2010). https://doi.org/10.1103/PhysRevA.82.064101

Li, T., Luo, L., Hupalo, M., Zhang, J., Tringides, M.C., Schmalian, J., Wang, J.: Femtosecond population inversion and stimulated emission of dense Dirac fermions in graphene. Phys. Rev. Lett. (2012). https://doi.org/10.1103/PhysRevLett.108.167401

Li, L., Lan, P., He, L., Zhu, X., Chen, J., Lu, P.: Scaling law of high harmonic generation in the framework of photon channels. Phys. Rev. Lett. (2018). https://doi.org/10.1103/PhysRevLett.120.223203

Lin, X., Li, R., Gao, F., Li, E., Zhang, X., Zhang, B., Chen, H.: Loss induced amplification of graphene plasmons. Opt. Lett. **41**(4), 681–684 (2016a)

Lin, X., Rivera, N., López, J.J., Kaminer, I., Chen, H., Soljačić, M.: Tailoring the energy distribution and loss of 2D plasmons. New J. Phys. (2016b). https://doi.org/10.1088/1367-2630/18/10/105007

Liu, Z., Zhang, Q., Liu, X., Yao, Y., Xiao, J.: Absence of exceptional points in square waveguide arrays with apparently balanced gain and loss. Sci. Rep. (2016). https://doi.org/10.1038/srep22711

Ni, G.X., Wang, L., Goldflam, M.D., Wagner, M., Fe, Z., McLeo, A.S., Liu, M.K., Keilman, F., Özyilmaz, B., Castro Neto, A.H., Hone, J., Fogler, M.M., Basov, D.N.: Ultrafast optical switching of infrared plasmon polaritons in high-mobility graphene. Nat. Photonics **10**, 244–247 (2016)

Orlova, A.A., Zhukovsky IV, S.V., Iorsha, P.A.Belov: Controlling light with plasmonic multilayers. Photonics Nanostruct. Fundam. Appl. **12**, 213–230 (2014)

Peng, L., Zhang, L., Yuan, J., Chen, C., Bao, Q., Qiu, C.W., Peng, Z., Zhang, K.: Gold nanoparticle mediated graphene plasmon for broadband enhanced infrared spectroscopy. Nanotechnology (2017). https://doi.org/10.1088/1361-6528/aa7453

Qin, C., Wang, B., Long, H., Wang, K., Lu, P.: Nonreciprocal phase shift and mode modulation in dynamic graphene waveguides. J. Lightwave Technol. **34**(16), 3877–3883 (2016)

Qin, C., Zhou, F., Peng, Y., Sounas, D., Zhu, X., Wang, B., Dong, J., Zhang, X., Alù, A., Lu, P.: Spectrum control through discrete frequency diffraction in the presence of photonic gauge potentials. Phys. Rev. Lett. (2018). https://doi.org/10.1103/PhysRevLett.120.133901

Sun, C., Rong, K., Wang, Y., Li, H., Gong, Q., Chen, J.: Plasmonic ridge waveguides with deep-sub-wavelength outside-field confinements. Nanotechnology (2016). https://doi.org/10.1088/0957-4484/27/6/065501

Wang, B., Zhang, X., García-Vidal, F.J., Yuan, X., Teng, J.: Strong coupling of surface plasmon polaritons in monolayer graphene sheet arrays. Phys. Rev. Lett. (2012). https://doi.org/10.1103/PhysRevLett.109.073901

Wang, Z., Wang, B., Long, H., Wang, K., Lu, P.: Surface plasmonic lattice solitons in semi-infinite graphene sheet arrays. J. Lightwave Technol. **35**(14), 2960–2965 (2017a)

Wang, F., Qin, C.Z., Wang, B., Long, H., Wang, K., Lu, P.X.: Rabi oscillations of plasmonic supermodes in graphene multilayer arrays. IEEE J. Sel. Top. Quantum Electr. (2017b). https://doi.org/10.1109/JSTQE.2016.2537205

Wang, S., Wang, B., Qin, C., Wang, K., Long, H.: Rabi oscillations of optical modes in a waveguide with dynamic modulation. Opt. Quantum Electron. (2017c). https://doi.org/10.1007/s11082-017-1220-3

Wang, Y., Guo, Y., Liao, H., Li, Z., Gan, F., Sun, C., Chen, J.: Multichannel and binary-phase all-optical control with on-chip integrated subwavelength plasmonic waveguides. ACS Photonics **5**(4), 1575–1582 (2018a)

Wang, F., Ke, S., Qin, C., Wang, B., Long, H., Wang, K., Lu, P.: Topological interface modes in graphene multilayer arrays. Opt. Laser Technol. **103**, 272–278 (2018b)

Xie, H., Li, M., Luo, S., Li, Y., Tan, J., Zhou, Y., Cao, W., Lu, P.: Photoelectron holography and forward scattering in atomic ionization by elliptically polarized laser pulses. Opt. Lett. **43**(14), 3220–3223 (2018)

Zhang, L., Zhang, Z., Kang, C., Cheng, B., Chen, L., Yang, X., Wang, J., Li, W., Wang, B.: Tunable bulk polaritons of graphene-based hyperbolic metamaterials. Opt. Express **22**(11), 14022–14030 (2014)

Zhao, D., Wang, Z., Long, H., Wang, K., Wang, B., Lu, P.: Optical bistability in defective photonic multi-layers doped by graphene. Opt. Quantum Electron. (2017). https://doi.org/10.1007/s11082-017-0999-2

Zhen, B., Hsu, C., Igarashi, Y., Lu, L., Kaminer, I., Pick, A., Chua, S., Joannopoulos, J.D., Soljačić, M.: Spawning rings of exceptional points out of Dirac cones. Nature **525**(7569), 354–358 (2015)